



**HAL**  
open science

## Study of the surface oxides and corrosion behaviour of an equiatomic CoCrFeMnNi high entropy alloy by XPS and ToF-SIMS

Luntao Wang, Dimitri Mercier, Sandrine Zanna, Antoine Seyeux, Mathilde Laurent-Brocq, Loic Perriere, Ivan Guillot, Philippe Marcus

### ► To cite this version:

Luntao Wang, Dimitri Mercier, Sandrine Zanna, Antoine Seyeux, Mathilde Laurent-Brocq, et al.. Study of the surface oxides and corrosion behaviour of an equiatomic CoCrFeMnNi high entropy alloy by XPS and ToF-SIMS. *Corrosion Science*, 2020, 167, pp.108507. 10.1016/j.corsci.2020.108507 . hal-02470246

**HAL Id: hal-02470246**

**<https://hal.science/hal-02470246>**

Submitted on 7 Feb 2020

**HAL** is a multi-disciplinary open access archive for the deposit and dissemination of scientific research documents, whether they are published or not. The documents may come from teaching and research institutions in France or abroad, or from public or private research centers.

L'archive ouverte pluridisciplinaire **HAL**, est destinée au dépôt et à la diffusion de documents scientifiques de niveau recherche, publiés ou non, émanant des établissements d'enseignement et de recherche français ou étrangers, des laboratoires publics ou privés.

## Study of the surface oxides and corrosion behaviour of an equiatomic

### CoCrFeMnNi high entropy alloy by XPS and ToF-SIMS

Luntao Wang<sup>1</sup>, Dimitri Mercier<sup>1\*</sup>, Sandrine Zanna<sup>1</sup>, Antoine Seyeux<sup>1</sup>, Mathilde Laurent-Brocq<sup>2</sup>, Loïc Perrière<sup>2</sup>, Ivan Guillot<sup>2</sup>, Philippe Marcus<sup>1\*</sup>

*1 Chimie ParisTech, PSL University, CNRS, Institut de Recherche de Chimie Paris, Physical Chemistry of Surfaces Group, 75005 Paris, France*

*2 Université Paris-Est Créteil, CNRS, ICMPE (UMR7182), 94320, Thiais, France*

#### Abstract

XPS and ToF-SIMS analysis have been combined with electrochemical measurements to determine the corrosion behavior of the equiatomic CoCrFeMnNi high entropy alloy. An XPS methodology based on analysis of the 3p core level spectra was developed to determine the composition and thickness of oxide films. Both native oxide (~1.4nm) and passive films (~1.6nm) formed in acidic medium are duplex, comprising Cr and Mn inner layer and Cr/Fe/Co mixture outer layer. No nickel is observed in the oxide layer. The effects of exposure of the native film to sulfuric acid and passivation under anodic polarization have been investigated.

Keywords: High entropy alloy; Oxide film; Passivation; XPS; ToF-SIMS

## 1. Introduction

Equiatomic high entropy alloys (HEAs), compared to the traditional alloys usually comprising a base metal and alloy elements, are a new class of alloys in which the distinction between major and minor elements is not relevant anymore. Indeed, they are composed of four, five or more metallic elements, in near equimolar concentration [1, 2]. For some compositions, depending mainly on the balance between the entropy of configuration of the solid solution and the enthalpy of mixing of the intermetallic [3, 4], HEAs form a single phase solid solution (without any intermetallic or other secondary phases), such as face-centered cubic (FCC) alloys elaborated from transition metals [5-8] and body-centered cubic (BCC) alloys elaborated from refractory metals [9-12]. The FCC CoCrFeMnNi HEA, which was first discovered by Brian Cantor et al. [13], has received a great deal of research interest due to its excellent mechanical properties [14-16]. Although this type of HEA has been developed since 2004, very little research focused on the corrosion behaviour of CoCrFeMnNi HEA [17-20].

\*Corresponding authors:

*E-mail addresses:* dimitri.mercier@chimieparistech.psl.eu (D. Mercier),  
philippe.marcus@chimieparistech.psl.eu (P. Marcus)

The CoCrFeNi alloy was reported to have good anti-corrosion properties due to the formation of a protective oxide film rich in Cr species [18]. Generally, for conventional alloys containing chromium, such as stainless steel and Ni-base alloys, a high corrosion resistance is provided by the Cr-rich oxide layer playing the role of a barrier against the attack of aggressive ions from the environment [21-25]. The impact of other elements at high contents (Co and Mn) in the bulk alloys has been rarely studied. Normally, for alloys with high contents of Mn (range from 21 to 28 wt%), the corrosion resistance will decrease caused by the instability of the Mn oxide in the film [26]. The high Co concentration (15%) will also decrease the corrosion resistance of the alloys [27]. The corrosion behavior of CoCrFeNi-based HEAs, including Al, Cu, W, Mo and Ru[28-33], has been studied. Lee et al. [28] investigated the corrosion performance of  $\text{Al}_x\text{CrFe}_{1.5}\text{MnNi}_{0.5(x=0,0.3,0.5)}$  HEAs in 1M NaCl solution, and the results demonstrated that the addition of Al to the alloys reduces the resistance to pitting corrosion. The addition of Al in the  $\text{Al}_x\text{CoCrFeNi}_{(x=0,0.25,0.5,1)}$  HEAs had a similar effect in chloride-containing solution, with Al leading to the formation of a porous passive film [29]. The corrosion behaviour of  $\text{FeCoNiCrCu}_{(x=0,0.5,1)}$  HEA was studied in sulfuric acid, and it was suggested that the corrosion resistance of the alloys was deteriorated by the segregation of Cu resulting in galvanic corrosion [31]. The  $\text{CoCrFeNiMo}_{(x=0.1-0.5\text{at}\%)}$  HEAs demonstrated good corrosion resistance in Cl-containing solution due to the beneficial effect of Mo[32]. Scully et al. [33] reported excellent passivity for 38Ni-21Cr-20Fe-13Ru-6Mo-2W HEA with the enrichment of Cr (48 at%) and small amount of Mo (8 at%) in the oxide film. Some recent work was focused on the corrosion behavior of CoCrFeMnNi HEA. For example, a comparison between a CoCrFeMnNi HEA and a commercial alloy (Hastelloy® C276) in 3.5wt% NaCl solution has demonstrated an improvement of the corrosion resistance properties for the HEA [34]. A similar comparison with a 304 stainless steel in sulfuric acid solution, showing relatively low anti-corrosion performance of the HEA, could be explained by a lower content of Cr oxide and large quantity of hydroxide in the passive film. Characterization of oxidized CoCrFeMnNi HEA in air from 500 to 900°C showed the dependence of the oxide film composition on oxidation temperature. The oxide film is mainly composed of  $\text{Mn}_2\text{O}_3$  with a thin inner Cr oxide at temperatures lower than 800°C, while at 900°C, the oxide film was composed of  $\text{Mn}_3\text{O}_4$  [35]. However, up to now, there is a limited number of investigations of the corrosion behavior of CoCrFeMnNi HEA related to modification of composition and structure of the surface oxide films.

In this paper, we investigate the corrosion behavior of an equimolar CoCrFeMnNi high entropy alloy using electrochemical measurements coupled with advanced surface characterization

techniques, including Time-of-Flight Secondary Ions Mass Spectrometry (ToF-SIMS) and X-ray Photoelectron Spectroscopy (XPS). Particularly, the composition of the surface oxide layers (native oxide and passive films) was determined using a new XPS approach based on the peak fitting of the 3p photopeaks.

## 2. Experimental procedures

### 2.1 Sample preparation

Pure Fe, Co, Cr, Ni and Mn ingots (purity exceeding 99.9 wt%) were used to prepare the HEA by high frequency electromagnetic induction melting in a water-cooled copper crucible under He atmosphere. Before melting, samples were prepared by mechanical polishing of raw materials. Afterwards, the ingot was shaped into a rod with a diameter of 13 mm and a length of around 8 cm by gravity casting. The cooling rate was estimated to be about  $10^3 \text{ K}\cdot\text{s}^{-1}$ . Finally, the samples were wrapped into a tantalum sheet, and were annealed at 1373 K during 13h under a He atmosphere to limit oxidation. At the end of the annealing, the samples were air quenched. The objective of this homogenization annealing is to eliminate the dendritic microstructure formed during casting process. To refine the grain size, HEA samples were rolled and then annealed at a temperature of 900°C for 30min under a He atmosphere, followed by air quenching. The average grain size of the HEA is  $\sim 30\mu\text{m}$ . Table 1 presents the measured chemical composition of the HEA in atomic percentage (measured by scanning electron microscopy coupled with Energy-dispersive X-ray spectroscopy (EDX)). As shown in previous papers[6, 36], the obtained CoCrFeMnNi is a face centered cubic solid solution, which is representative of the high temperature (i.e.: 1373 K) stable state.

Elements	Fe	Co	Ni	Cr	Mn
at. %	19.8	20	19.9	20.3	20

**Table 1** Chemical composition of the CoCrFeMnNi alloy obtained by EDX

The samples were ground with SiC paper from 320 up to 2400 grit, and then polished with  $6\mu\text{m}$ ,  $3\mu\text{m}$ ,  $1\mu\text{m}$  and  $0.25\mu\text{m}$  diamond suspension until a mirror like finish is obtained. They were then cleaned in ultrasonic baths of acetone, ethanol and ultra-pure water for 10 mins, and dried in compressed air. The sample surfaces were mechanically polished before each electrochemical experiment.

### 2.2 Electrochemical measurements

A three-electrode cell comprising a saturated calomel reference electrode (SCE,

+0.245V/NHE), a Pt wire as the counter electrode and a HEA sample as a working electrode (area 1.3cm<sup>2</sup> delimited by a Viton O ring) was used. The electrochemical measurements were carried out at room temperature in 0.05 M H<sub>2</sub>SO<sub>4</sub> (aq) prepared with ultra-pure water (Millipore, resistivity 18.5Mohm.cm) pre-deaerated by Ar bubbling for 30 min. An EC\_Lab SP200 potentiostat from Bio-Logic was used. Before the potentiodynamic and potentiostatic tests, the open circuit potential (OCP) was monitored for 30 min, corresponding to the stabilisation time of the potential. The potentiodynamic polarization tests were performed at a potential scan rate of 1 mV.s<sup>-1</sup>, and the potential range was from -800mV/SCE to 1200mV/SCE. The potentiostatic tests were carried out at 200mV/SCE, 400mV/SCE and 600mV/SCE.

### **2.3 Surface characterization**

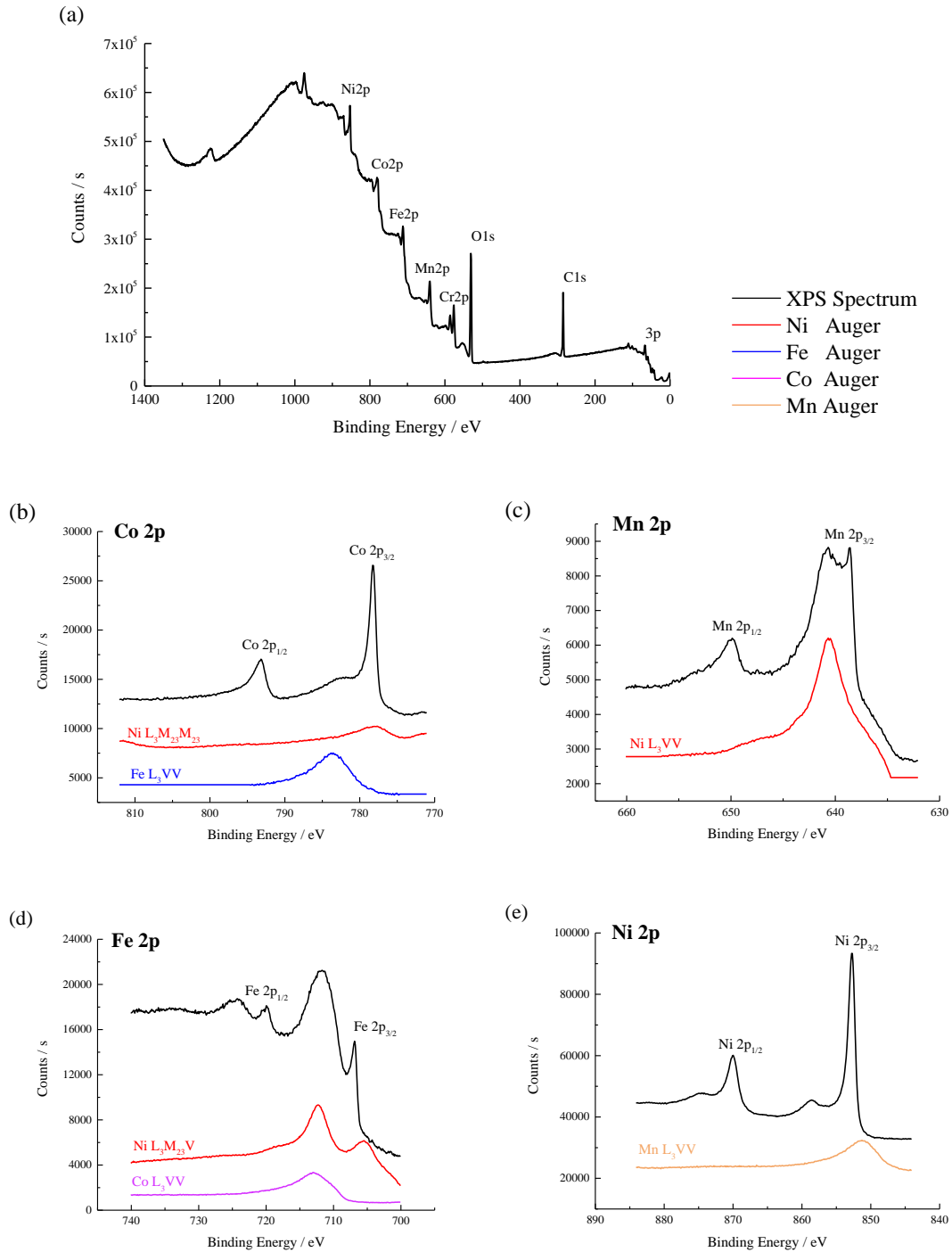
Surface analysis was performed by a combination of X-Ray Photoelectron Spectroscopy (XPS), and Time-of-Flight Secondary Ions Mass Spectrometry (ToF-SIMS).

X-ray Photoelectron Spectroscopy (XPS) analysis was performed using a Thermo Electron Escalab 250 spectrometer, with a monochromatic Al K $\alpha$  X-ray source ( $h\nu=1486.6\text{eV}$ ) operating at a pressure around 10<sup>-9</sup> mbar. The analyser pass energy was 50eV for survey spectra and 20eV for high resolution spectra. Beforehand the spectrometer was calibrated using Au4f<sub>7/2</sub> at 84.1eV. Spectra were recorded and analysed using Thermo *Avantage* software (Version 5.956).

Elemental depth profiles were obtained using a ToF-SIMS 5 spectrometer (IONTOF GmbH). The spectrometer was run at an operating pressure of 10<sup>-9</sup> mbar. A pulsed 25 keV Bi<sup>+</sup> primary ion source was employed for analysis, delivering a current of 1.2 pA over a 100 × 100  $\mu\text{m}^2$  area. Depth profiling was carried out by interlacing static analysis with sputtering using a 0.5 keV Cs<sup>+</sup> sputter beam giving a 17 nA target current over a 300×300  $\mu\text{m}^2$  area.

# 3. Results

## 3.1 The native oxide film



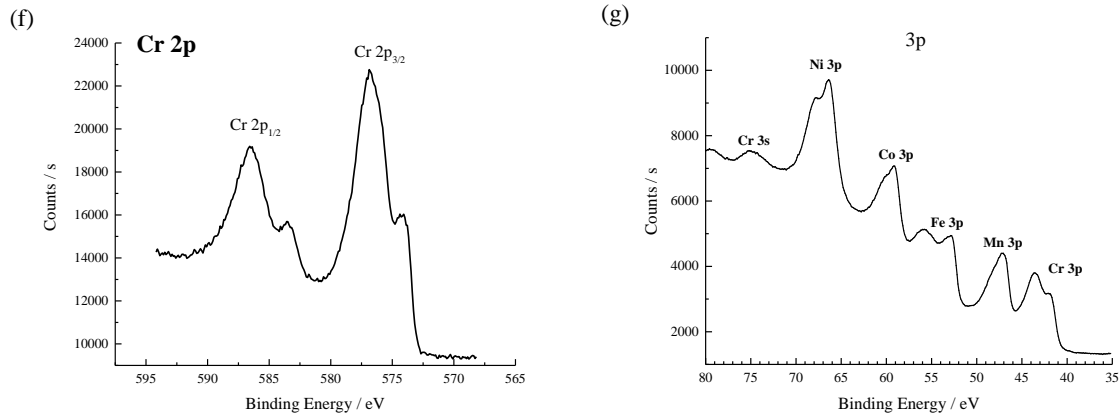


**Fig.1** High resolution XPS (a) survey spectrum, (b)-(f) 2p core level spectra and (g) 3p core level spectrum recorded for the native oxide film formed on the HEA and Auger transitions of pure elements constituting the CoCrFeMnNi alloy

X-Ray Photoelectron Spectroscopy (XPS) is an appropriate method to investigate the composition of nanometer-thick surface oxide films[21, 22, 37-40]. Generally, for alloys containing Fe, Cr, Ni, Co and Mn, the 2p core level peaks are recorded with high resolution and many references are available to study the chemical states of the analyzed elements[41-46]. However, for the CoCrFeMnNi HEA with five elements in equiatomic ratios, new challenges appear to analyze the XPS data due to the interference of the Auger transitions which overlap with 2p peaks of the main elements in the alloy.

The characteristic high resolution XPS 2p core level spectra obtained for a native oxide film formed on the equiatomic CoCrFeMnNi HEA are presented on Fig.1(b)-(f). For each spectrum, the Auger transitions of constituting elements of the HEA have been added. It is observed that using the Al K $\alpha$  X-ray source all photopeaks overlap with Auger transitions except the Cr 2p<sub>3/2</sub> peak (Co2p<sub>3/2</sub> / NiL<sub>3</sub>M<sub>23</sub>M<sub>23</sub> and FeL<sub>3</sub>VV, Mn2p<sub>3/2</sub> / NiL<sub>3</sub>VV, Fe2p<sub>3/2</sub> / NiL<sub>3</sub>M<sub>23</sub>V and CoL<sub>3</sub>VV, Ni2p<sub>3/2</sub> / MnL<sub>3</sub>VV). An Mg K $\alpha$  X ray source could be used, but overlap with Auger transitions (Fe2p<sub>3/2</sub> / Mn L<sub>3</sub>M<sub>23</sub>M<sub>23</sub>) still exist making quantification difficult.

Thus, another approach based on the 3p core level peaks (Fig.1(g)) was developed to characterize the HEA surfaces. Although the sensitivity of 3p peaks is lower than for 2p peaks, the 3p spectra do not present overlapping with Auger peaks and the narrow energy range for the analyzed elements allows probing the same thickness for all elements.

To develop this new approach, a new database for 3p core level spectra must be established.

		BE (eV)	FWHM (eV)	L/G Mix (%)	Tail Mix (%)	Tail Height (%)	Tail Exponent
Metal	Cr3p <sub>(met)</sub>	41.62	1.21	30.26	0.01	0.15	0.0929
	Mn3p <sub>(met)</sub>	46.78	1.09	37.8	0	0.02	0.0926
	Fe3p <sub>(met)</sub>	52.65	0.96	10.9	0.33	99.97	0.0545
	Co3p <sub>(met)</sub>	58.94	1.26	85.89	8.63	0	0.0431
	Ni3p <sub>3/2(met)</sub>	66.25	2.06	60.54	0	0.12	4.0958
	Ni3p <sub>1/2(met)</sub>	68.1	2.06	60.54	0	0.12	4.0958
Oxide	Cr3p <sub>(ox)</sub>	43.72	2.4	30	100	0	0
	Cr3p <sub>(hyd)</sub>	44.45	2.4	30	100	0	0
	Mn3p <sub>(ox)</sub>	48.09	2.4	30	100	0	0
	Fe3p <sub>(ox)</sub>	54.73	2.9	30	100	0	0
	Co3p <sub>(ox)</sub>	59.74	2.2	30	100	0	0

**Table 2** The parameters for fitting the XPS 3p spectra of the pure metals and oxides

Firstly, the standard 3p core level peaks for the pure metals were recorded using pure metals from batches used to manufacture the CoCrFeMnNi HEA. These pure metal samples were polished with 2400 grit SiC paper, and then introduced into the XPS analysis chamber. Samples were sputtered using an Ar<sup>+</sup> ion beam to remove surface oxides and contaminants and obtain metallic surfaces. High resolution XPS 3p core level spectra were recorded and curve fitted using the Thermo Electron software Avantage with an iterative Shirley-type background subtraction. All the parameters, including binding energy (BE), full width at half maximum (FWHM), Gaussian-Lorentzian(GL) ratio and asymmetry factor, were automatically adjusted by the software to best fit the peaks of pure metals. An asymmetric function was necessary for the peak fitting of metal peaks, as expected for transition metals (owing to the conduction electron scattering amplitude for inter-band absorption or emission in metals, at the Fermi level[47, 48]). The detailed parameters for fitting the 3p peaks of pure metals are shown in Table 2. For Ni 3p, a splitting of the metallic component is observed (spin orbit coupling is due to the coupling between the electron spin momentum and its orbital angular momentum). Generally, this effect is visible for p, d and f core levels but spectral resolution can limit this splitting. It is the case here for the 3p orbitals of Cr, Mn, Fe and Co.

A similar approach based on the decomposition of the native oxide covering the pure metals has also been used. For components characteristic of the oxide layer, a Lorentzian/Gaussian peak shape with a fixed ratio of 30/70 was used. The detailed parameters for fitting the 3p peaks of oxides are shown in Table 2.



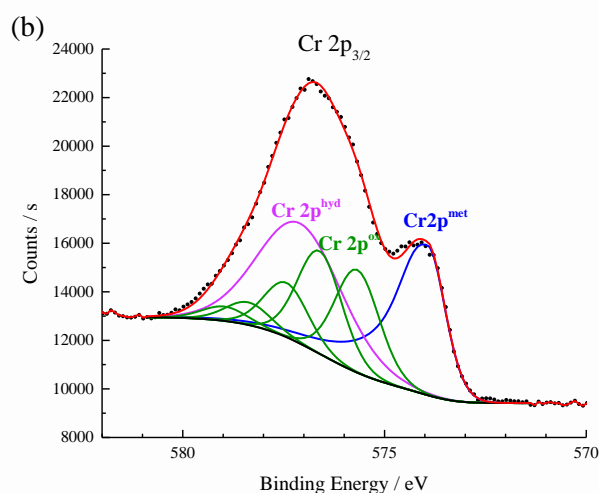
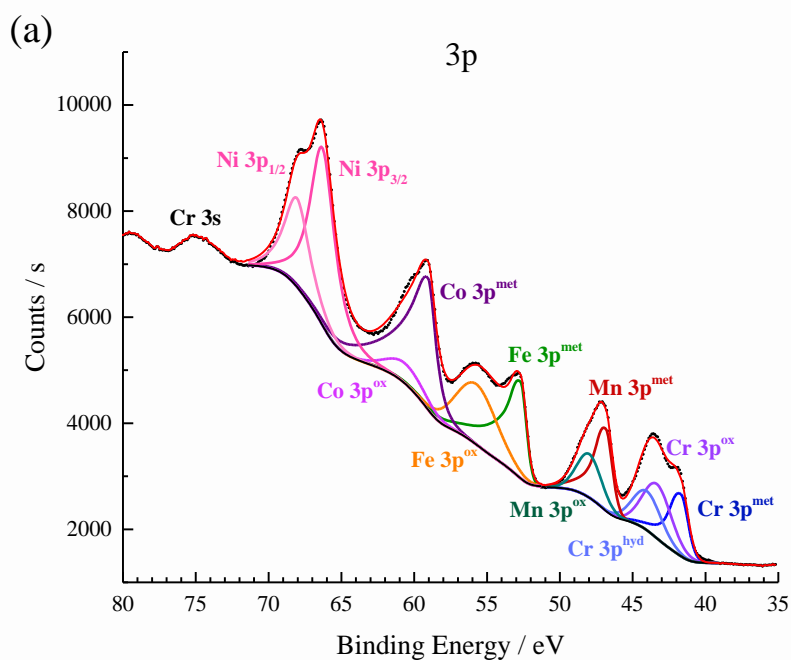


**Fig.2** XPS core level spectra for the native oxide film formed on the HEA: (a) Cr 3p, Mn 3p, Fe 3p, Co 3p, Ni 3p and (b) Cr 2p<sub>3/2</sub>. The black dots represent the experimental spectra and the colored lines show the peak fitting.

The spectrum (35-75eV) characteristic of the 3p peaks of Cr, Mn, Fe, Co and Ni, and the peak fitting for a native oxide film formed on CoCrFeMnNi HEA surface are presented in Fig.2(a). This decomposition has been carried out by introducing the fit parameters determined previously for each element (metal state and oxide state) (Table 2).

The Cr 3p core level spectrum is fitted with three peaks, corresponding to metallic Cr<sub>met</sub> (BE=41.6±0.1eV), oxide Cr<sub>ox</sub> (BE=43.7±0.1eV) and hydroxide Cr<sub>hyd</sub> (BE=44.4±0.1eV)

chemical states. As previously indicated, the absence of overlap between the Cr 2p<sub>3/2</sub> core level spectrum and Auger transitions of other metals makes it possible to decompose the Cr 2p<sub>3/2</sub> photopeak and compare the decomposition of the Cr 3p core level. Fig.2(b) shows the fitting of Cr 2p<sub>3/2</sub> core level spectrum. The Cr 2p<sub>3/2</sub> spectrum is fitted by three components characteristic of metallic Cr<sub>met</sub> (BE=573.9±0.1eV, FWHM=1.25eV), hydroxide Cr<sub>hyd</sub> (BE=577.1±0.1eV, FWHM=2.55eV) and oxide, which is represented by five peaks, based on the peak fitting method proposed by Biesinger [41], Cr<sub>ox</sub> (BE=575.7±0.1eV, 576.6±0.1eV, 577.4±0.1eV, 578.4±0.1eV and 579±0.1eV, FWHM=1.05eV). In our work, the area ratio between the 5 components of decomposed Cr 2p<sub>3/2ox</sub> (chromium oxide) has been determined and considered as fixed for all analysed surfaces.

The Co 3p, Fe 3p and Mn 3p spectra show two components representing the metallic states Co<sub>met</sub> (BE=58.9±0.1eV), Fe<sub>met</sub> (BE=52.7±0.1eV) and Mn<sub>met</sub> (BE=46.8±0.1eV), and the oxide states Co<sub>ox</sub> (BE=59.7±0.1eV), Fe<sub>ox</sub> (BE=54.7±0.1eV) and Mn<sub>ox</sub> (BE=48.1±0.1eV). The decomposition of Ni 3p into two components, Ni 3p<sub>3/2</sub> at 66.3eV and Ni 3p<sub>1/2</sub> at 68.1eV only shows the presence of metallic nickel underneath the oxide layer. No oxidized nickel is observed in the surface oxide layer.

To calculate the thickness of the oxide film and the chemical composition of the film and the modified alloy layer under the oxide, a model consisting in a homogeneous and continuous oxide layer on the sample surface, comprising Fe<sub>ox</sub>, Cr<sub>ox/hyd</sub>, Mn<sub>ox</sub> and Co<sub>ox</sub>, and a modified alloy layer with Fe<sub>met</sub>, Cr<sub>met</sub>, Mn<sub>met</sub>, Co<sub>met</sub> and Ni<sub>met</sub> was assumed. Based on this model, the following 11 equations with 11 unknowns ( $k, d_{oxide}, D_{Cr}^{Met}, D_{Mn}^{Met}, D_{Fe}^{Met}, D_{Co}^{Met}, D_{Ni}^{Met}, D_{Cr}^{Ox}, D_{Mn}^{Ox}, D_{Fe}^{Ox}, D_{Co}^{Ox}$ ) was used :

$$I_X^{Met} = k\sigma_X\lambda_X^{Met}D_X^{Met}T_X\exp\left(-\frac{d_{oxide}}{\lambda_X^{Ox}}\right), \text{ with X=Cr, Mn, Fe, Co and Ni} \quad (1)$$

$$I_Z^{Ox} = k\sigma_Z\lambda_Z^{Ox}D_Z^{Ox}T_Z\left[1 - \exp\left(-\frac{d_{oxide}}{\lambda_Z^{Ox}}\right)\right], \text{ with Z=Cr, Mn, Fe and Co} \quad (2)$$

$$D_{Cr}^{Met} + D_{Mn}^{Met} + D_{Fe}^{Met} + D_{Co}^{Met} + D_{Ni}^{Met} = D^{Met} \quad (3)$$

$$D_{Cr}^{Ox} + D_{Mn}^{Ox} + D_{Fe}^{Ox} + D_{Co}^{Ox} = D^{Ox} \quad (4)$$

with  $I_X^Y$  the intensity of photoelectrons (cps eV) emitted by the considered core level X in the matrix Y,  $k$  a constant characteristic of the spectrometer,  $\sigma_X$  the photoionization cross-section of the considered core level X,  $\lambda_X^Y$  the inelastic mean free path of photoelectrons emitted by the considered core level X in the matrix Y (in nm),  $T_X$  the transmission function of the analyse for the considered core level X,  $d_{oxide}$  the thickness of the oxide layer (nm)

and  $D_X^Y$  the density of the element X in the matrix Y ( $\text{mol.cm}^{-3}$ ) defined by  $D_X^Y = \frac{\rho_Y}{M_Y} \times x_X^Y$  with  $\rho_Y$  the density of the matrix Y ( $\text{g.cm}^{-3}$ ),  $M_Y$  the molar mass of the matrix Y ( $\text{g.mol}^{-1}$ ) and  $x_X^Y$  the atomic percentage of the element X in the matrix Y. The  $\rho_{Met}$  value is  $8 \text{ g.cm}^{-3}$  [49, 50]. The  $\rho_{Ox}$  value is taken as  $5.22 \text{ g.cm}^{-3}$ , which is the density of chromium oxide, as it is shown later that the surface oxide layer is enriched in Cr(III). The density of  $\text{Fe}_2\text{O}_3$  would be similar ( $5.24 \text{ g.cm}^{-3}$ ). The values of the photoionization cross-sections ( $\sigma_X$ ) at 1486.6 eV are taken from Scofield[51] and the inelastic mean free paths ( $\lambda_X^Y$ ) calculated by the TPP2 formula[52] are compiled in the Table 3.

Core level	Cr 3p	Mn 3p	Fe 3p	Co 3p	Ni 3p
$\sigma_X$	1.173	1.423	1.669	1.93	2.217
$\lambda_X^{oxide}(\text{nm})$	2.6	2.6	2.59	2.58	2.57
$\lambda_X^{metal}(\text{nm})$	2.14	2.14	2.14	2.14	2.14

**Table 3** Values of the photoionization cross-section ( $\sigma_X$ ) and inelastic mean free paths ( $\lambda_X^Y$ ) used for XPS quantification

Using the intensities of the 3p peaks obtained after peak fitting and equations (1) to (4), the thickness of the oxide layer as well as the elemental compositions of the oxide layer and of the modified layer under the oxide (alloy/oxide interface) are determined. The results are reported in Table 4.

	Thickness(nm)	Oxide composition(Atomic%)					Modified alloy composition(Atomic%)				
		Cr <sub>(ox)</sub>	Cr <sub>(hyd)</sub>	Mn <sub>(ox)</sub>	Fe <sub>(ox)</sub>	Co <sub>(ox)</sub>	Cr <sub>(met)</sub>	Mn <sub>(met)</sub>	Fe <sub>(met)</sub>	Co <sub>(met)</sub>	Ni <sub>(met)</sub>
Native oxide	1.4	26.5	19.8	15.2	30.3	8.2	11.7	12.5	17.1	24.9	33.8
OCP 1min	1.4	30.4	26.0	18.5	13.9	11.2	15.6	12.4	17.8	19.5	34.7
OCP 30min	1.8	36.5	31.4	19.0	8.7	4.5	16.6	15.0	16.9	21.3	30.2
OCP 60min	2	36.2	32.9	16.7	8.0	6.2	16.8	16.3	17.9	17.6	31.5
Passivation 200mV	1.6	48.8	13.8	18.1	14.2	5.2	16.2	15.3	18.2	21.3	29.1
Passivation 400mV	1.7	53.4	11.8	13.1	16.4	5.4	16.8	15.4	18.0	20.6	29.1
Passivation 600mV	1.6	49.2	19.7	14.4	12.2	4.6	16.3	14.9	18.4	20.7	29.8
Passivation(400mV) 10 $\mu$ A	1.6	35.5	32.2	11.0	16.4	5.0	16.8	16.6	17.3	21.0	28.4
Passivation(400mV) 1 $\mu$ A	1.6	48.7	19.2	12.9	14.0	5.2	16.5	15.7	18.1	21.0	28.7
Passivation(400mV) 0.1 $\mu$ A	1.7	53.4	11.8	13.1	16.4	5.4	16.8	15.4	18.0	20.6	29.1

**Table 4** Thickness and chemical composition of the native oxide, the oxide after exposure to acidic solution at the open circuit potential (OCP) and passive films formed in 0.05M  $\text{H}_2\text{SO}_4$  on equiatomic CoCrFeMnNi HEA surface

The thickness for the native oxide film is estimated at 1.4 nm. The native oxide film presents a strong enrichment of chromium (46.3 at%, including 26.5 at% of oxide and 19.8 at% of hydroxide) and iron (30.3 at%) while a depletion of Co (8.2 at%) is clearly observed. No nickel oxide is detected by XPS in the oxide layer.

In the modified metallic alloy layer under the native oxide, a depletion of metallic Cr (11.7

at%), Mn (12.5 at%) and Fe (17.1 at%) is observed, while the concentration of metallic Ni (33.8 at%) and Co (24.9 at%) are significantly higher than in the bulk. The chromium depletion zone in the modified alloy layer is correlated to the enrichment of chromium oxide in the oxide film. The chromium enrichment in the oxide is due to the higher oxygen affinity to Cr [53] (standard free energy of formation for chromium oxide ( $\Delta G_{298.15\text{K}}$ ) is -1058.067 kJ/mol [54], i.e more negative than for the other alloy elements). A Cr depleted-zone in the alloy beneath the oxide film appears due to slow diffusion in the alloy matrix at room temperature [55, 56].

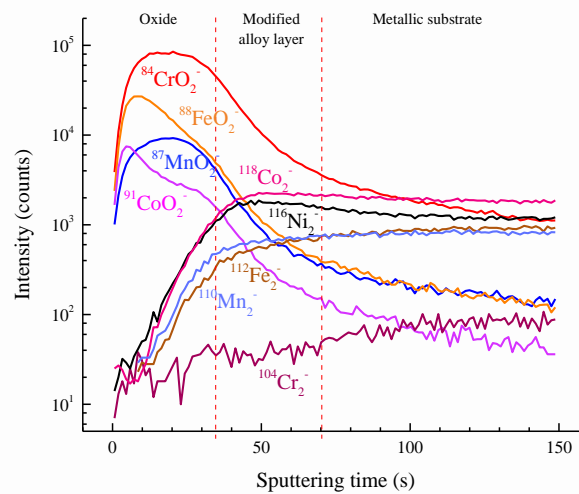


Fig.3 ToF-SIMS depth profiles for the native oxide film formed on the HEA

Fig.3 shows the ToF-SIMS negative ion depth profiles for the native oxide film formed on the surface of the HEA sample. The intensity is plotted in logarithmic scale versus sputtering time. The  $^{84}\text{CrO}_2^-$  ion profile is used to define the oxide film region (ending at 84% of the maximum intensity in the depth profile) since the chromium oxide is located throughout the oxide film region, and the  $^{112}\text{Fe}_2^-$  ion profile is used to define the metallic region (starting at beginning of the intensity plateau). Thus, an intermediate region is determined from 35s to 70s of sputtering. The colour dashed lines mark the limits between the oxide film, modified alloy layer and metallic substrate.

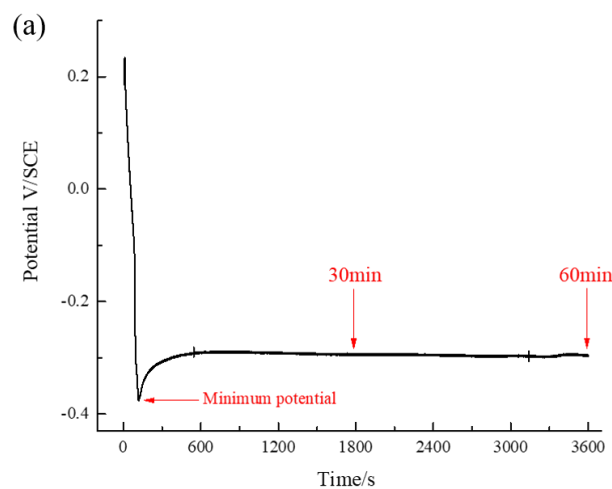
In the oxide region, one observes that the  $^{88}\text{FeO}_2^-$  profile peaks in the outer part of the oxide film region and decreases slowly through the oxide. Oxidized iron is therefore mainly located in the outer part of the film, although its presence in small amount in the inner oxide cannot be excluded. The  $^{91}\text{CoO}_2^-$  profile also has its maximum in the outer region of the oxide film, indicating that the cobalt oxide is mainly located in the outer oxide. Furthermore,  $^{91}\text{CoO}_2^-$  appears to peak before the maximum intensity of the  $^{88}\text{FeO}_2^-$  signals, indicating that Co oxide

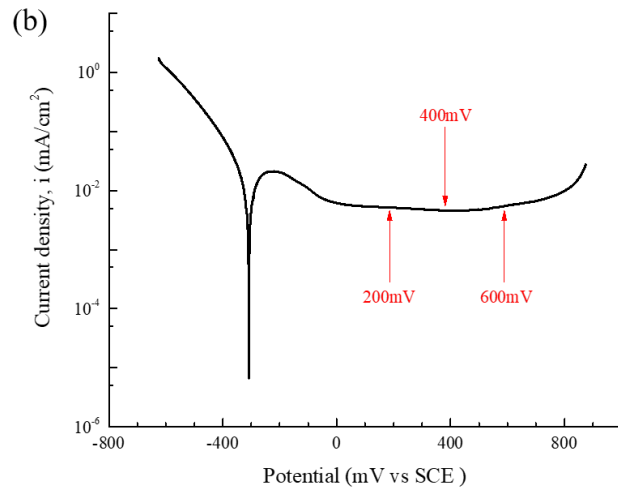
is the main species at the surface. The  $^{84}\text{CrO}_2^-$  profile exhibits a wide peak throughout the whole region of the film. Oxidized chromium is thus distributed in the whole film. Finally, the  $^{87}\text{MnO}_2^-$  profile has its maximum in the inner region of the oxide film (around 20s of sputtering time), indicating that manganese oxide is preferentially located in the inner oxide film region. The  $^{90}\text{NiO}_2^-$  ion is not plotted in Fig.1, since its intensity is extremely low compared to those of  $^{84}\text{CrO}_2^-$ ,  $^{88}\text{FeO}_2^-$ ,  $^{91}\text{CoO}_2^-$  and  $^{87}\text{MnO}_2^-$  ions. It means that Ni oxide is present only at trace level in the oxide film.

Focussing on the intermediate region, one can see that it is characterised by increasing intensities of the signals of the metallic compounds ( $^{112}\text{Fe}_2^-$ ,  $^{110}\text{Mn}_2^-$ ,  $^{116}\text{Ni}_2^-$  and  $^{118}\text{Co}_2^-$ ) and a fast decrease of the intensity of the signals characteristic of the oxides, i.e.  $\text{MO}_2^-$  (with  $\text{M}=\text{Cr}$ ,  $\text{Fe}$ ,  $\text{Mn}$ ,  $\text{Co}$ ), making the passage of the oxide/alloy interface. The alloy region under the oxide is enriched in Ni and Co, as indicated by the hump in the  $\text{Ni}_2^-$  and  $\text{Co}_2^-$  signals. The  $^{104}\text{Cr}_2^-$  profile shows very low intensity due to low secondary emission yield.

From ToF-SIMS observations, it is thus possible to establish the presence of a duplex oxide structure composed of chromium, iron and cobalt oxides in the outer layer and chromium and manganese oxides in the inner layer. Under this duplex oxide film, near the metal/oxide interface, there is a modified alloy layer, enriched in Ni and Co. The alloy substrate can be located for sputtering times over 70s.

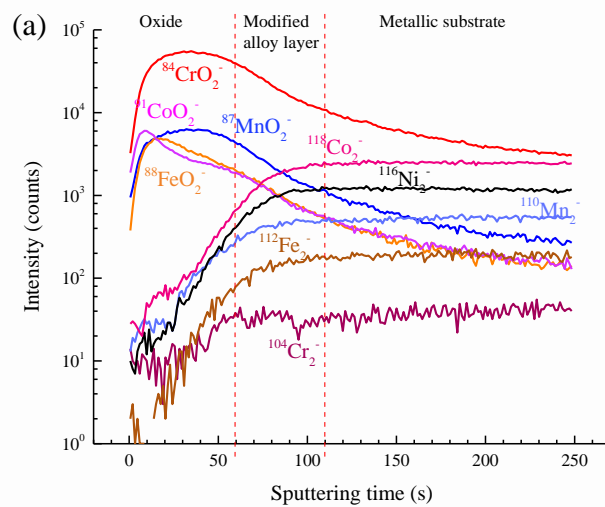
### 3.2 Surface oxide film after exposure to acidic aqueous solution at the open circuit potential





**Fig.4 (a)** Open circuit potential evolution for the CoCrFeMnNi HEA with a native oxide film in 0.05M H<sub>2</sub>SO<sub>4</sub> and **(b)** Potentiodynamic polarization curve of the CoCrFeMnNi HEA in 0.05M H<sub>2</sub>SO<sub>4</sub> (scan rate of 1mV/s)

The evolution of the open circuit potential (OCP) for the CoCrFeMnNi HEA with a native oxide film in 0.05M H<sub>2</sub>SO<sub>4</sub> electrolyte is presented in Fig.4(a). The potential exhibits a sharp decrease and reaches its minimum value after ~1min of immersion, suggesting some dissolution of the native film. Then the potential increases slightly to reach a stabilisation plateau after 600s. In order to determine the chemical changes at the surface during immersion at OCP, surfaces immersed for 1min (minimum potential), 30 and 60 min were analysed by XPS and ToF-SIMS. The XPS data are compiled in Table 4 and ToF-SIMS profiles are presented on Fig.5.



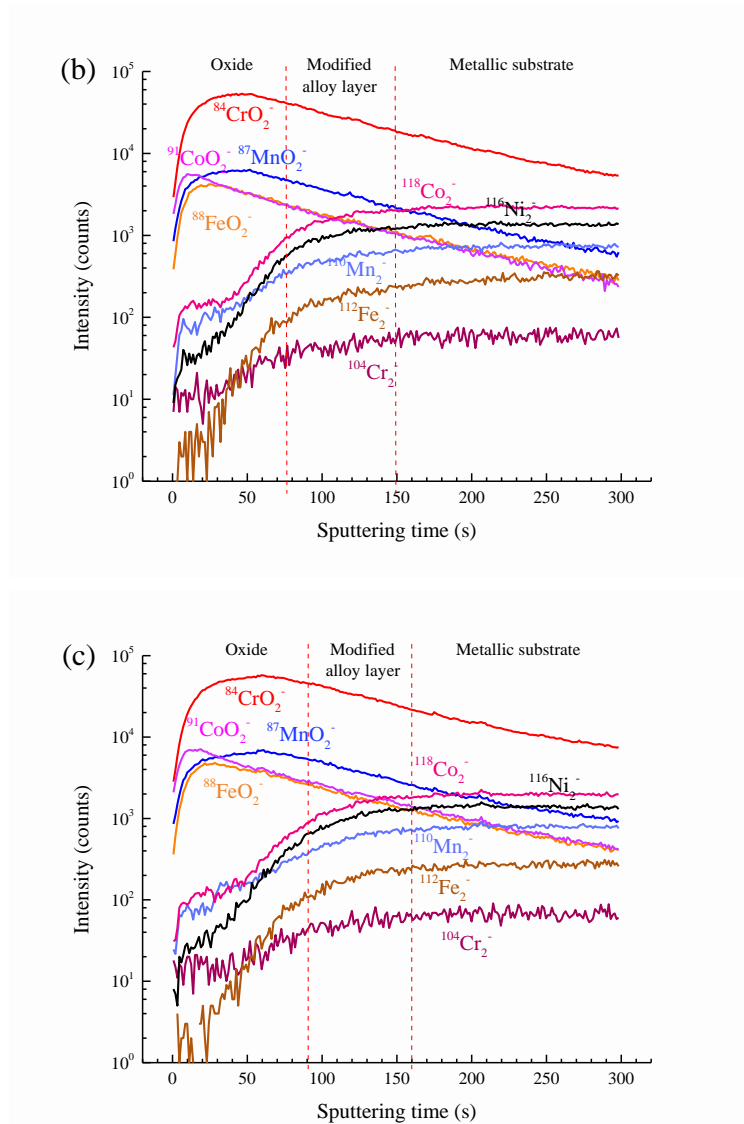


**Fig.5** ToF-SIMS depth profiles for the HEA with a native oxide film after exposure to 0.05M H<sub>2</sub>SO<sub>4</sub> at OCP for (a) 1min, (b) 30min and (c) 60min

Fig.5 shows ToF-SIMS depth profiles obtained on HEA samples after exposure to acidic aqueous solution at the OCP. The general behaviour is similar to the one observed on the native oxide. Fe and Co oxides are located in the outer layer while Mn oxide is in the inner layer. Cr oxide is distributed in the whole film. The maximum intensity of  $^{88}\text{FeO}_2^-$  strongly decreases with increasing immersion time (compared to the native oxide) indicating a decrease of the iron content in the outer oxide.

The sputtering time associated to the thickness of the oxide layer is increasing from 60s to 90s for 1min and 60min immersion in acidic aqueous solution at OCP, meaning that the thickness of the oxide film is increasing with prolonged immersion time, which is in agreement with XPS data (1.4 and 2 nm, respectively).

The immersion time in sulfuric acid has also an effect on the shape of the oxide depth profiles. For all characteristic ions of the oxides, a slow decrease of the signal is observed in the metallic substrate region. This indicates a roughening of the metal/oxide interface.

The chemical composition and thickness of the film and modified alloy layer for different immersion times in 0.05M H<sub>2</sub>SO<sub>4</sub> are reported in Table 4. Although the thickness of the film after 1 minute of immersion is similar to the one of the native oxide layer, the chemical composition is strongly modified. A sharp decrease of iron content is observed (13.9 at% compared to 30.3 at% for the native oxide), which can be explained by the dissolution of iron oxide during the immersion in acidic solution. The content of chromium compounds, and particularly the chromium hydroxide, increases strongly (26.0 at% as compared to 19.8 at% for the native oxide). For increasing immersion time at the open circuit potential, the amount of iron in the oxide layer continues to decrease until it becomes stationary (8.7 at% after 30min and 8.0 at% after 1h), and the amount of chromium in the oxide film continues to increase until it becomes stationary (Cr oxide: 36.5 at% for 30min and 36.2 at% after 1h; Cr hydroxide: 31.4 at% for 30min and 32.9 at% after 1h). During the immersion, the amounts of cobalt and manganese oxides remain nearly constant. Nickel oxide is not detected. A thickening of the oxide layer is observed during the immersion.

### **3.3 Passivity of the HEA alloy**

To further understand the reactivity of the CoCrFeMnNi HEA surfaces, different passive layers have been elaborated by chronoamperometry in 0.05M H<sub>2</sub>SO<sub>4</sub>. The experimental parameters for the formation of passive layers have been determined from potentiodynamic polarization curves in 0.05M H<sub>2</sub>SO<sub>4</sub> solution, presented in Fig.4(b) for a scan rate of 1 mV.s<sup>-1</sup>. In the anodic region, the HEA shows an anodic current peak at -250mV/SCE caused by active dissolution, then a wide passive range from 0mV/SCE to 800mV/SCE. The lowest current density is observed at 400mV/SCE. To investigate the passive state of the HEA, it was maintained in 0.05M H<sub>2</sub>SO<sub>4</sub>(aq) at a passive potential until current went down to 0.1μA/cm<sup>2</sup> for three different passive potentials (200 mV, 400 mV and 600 mV). The passive film and the alloy underneath the film were subsequently analysed by XPS, and the XPS 3p core level spectra for the passive films formed on the HEA for three different passive potentials are shown in Fig.6.



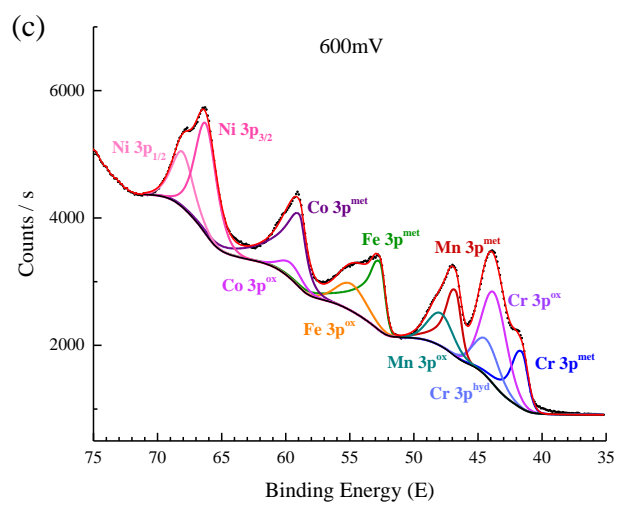
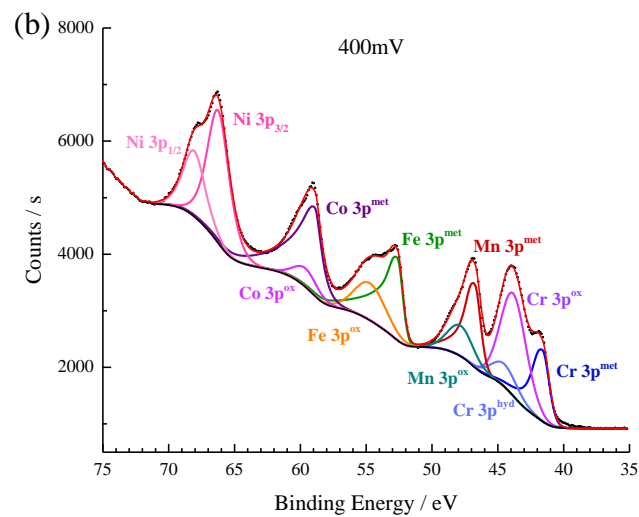
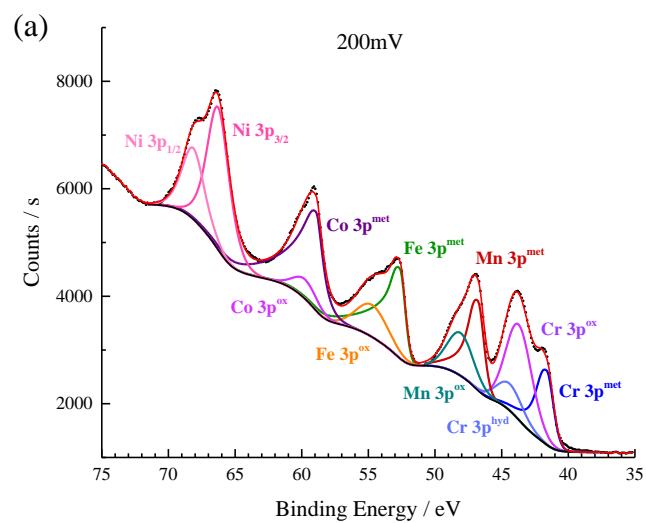


**Fig.6** XPS 3p core level spectra for the passive films formed on the HEA at three different passive potentials:(a) 200 mV, (b) 400 mV and (c) 600 mV

The results of composition and thickness of the passive films, obtained from the XPS 3p core level spectra, are reported in Table.4. The thickness of the passive films is found to be 1.6 nm after passivation at 200mV and 600mV, and 1.7 nm at 400mV. Thus, the passivation potential has no significant effect on the thickness of the film. In the passive film a chromium enrichment is always observed compared to the native oxide. This enrichment is mainly reflected in a strong increase of the chromium oxide (48.8 at% at 200 mV, 53.4 at% at 400 mV and 49.2 at% at 600mV compared to 26.5 at% for the native oxide) while chromium hydroxide is in average slightly lower (13.8 at% at 200 mV, 11.8 at% at 400 mV and 19.7 at% at 600mV) than in the native oxide (19.8 at%). The amounts of Mn and Co measured in the passive film are similar to those measured in the native oxide. The iron content shows a strong decrease, which was also observed at the OCP, assigned to a selective dissolution of iron oxide.

The Cr, Mn and Fe contents in the modified alloy layer under the passive film are found to be around 16 at%, 15 at% and 18 at%, respectively. This shows a slight depletion of Cr, Mn and Fe in the modified alloy layer compared to the contents in the bulk. The concentrations of Co in the modified alloy region are found to be around 20 at%, i.e. similar to the Co bulk content. The Ni contents in the modified alloy layer reach 29 at%, revealing a strong Ni enrichment under the oxide compared to the bulk (20 at%). The composition of the modified alloy layer under the passive film is similar to the one of the native oxide. It is to be noted that despite the stronger enrichment of chromium oxide in the passive film compared to the native oxide, the content of Cr (16 at%) in the modified alloy layer is slightly higher than that for the native oxide (12 at%). This is related to the passivation process in which there is no dissolution of Cr, whereas Fe is dissolved.

Table 4 also shows the composition and thickness obtained for the passive film formed at 400mV at different passive currents. Increasing the passivation time at 400mV causes a decrease of the passive current. The passive film was analysed at three different stages (10 $\mu$ A/cm<sup>2</sup> (45s), 1 $\mu$ A/cm<sup>2</sup> (530s) and 0.1 $\mu$ A/cm<sup>2</sup> (4600s)). The thickness of the films remains unchanged (1.6 nm) with increasing passivation time (decreasing passive current). As for the concentration of the oxides in the film, the contents of Mn oxide (11 to 13 at%), Fe oxide (14 to 16 at%), Co oxide (5 at%) do not change significantly during prolonged passivation. The marked modification occurring in the film during the passivation is the increase of the Cr oxide (from 35.5 at% to 53.4 at%) combined with the decrease of the Cr hydroxide (from 32.2 at%

to 11.8 at%), indicating dehydroxylation during the passivation process. In the modified alloy layer, the fractions of metallic Cr (16 at%), Mn (16 at%), Fe (18 at%), Co (21 at%) and Ni (29 at%) are stable.

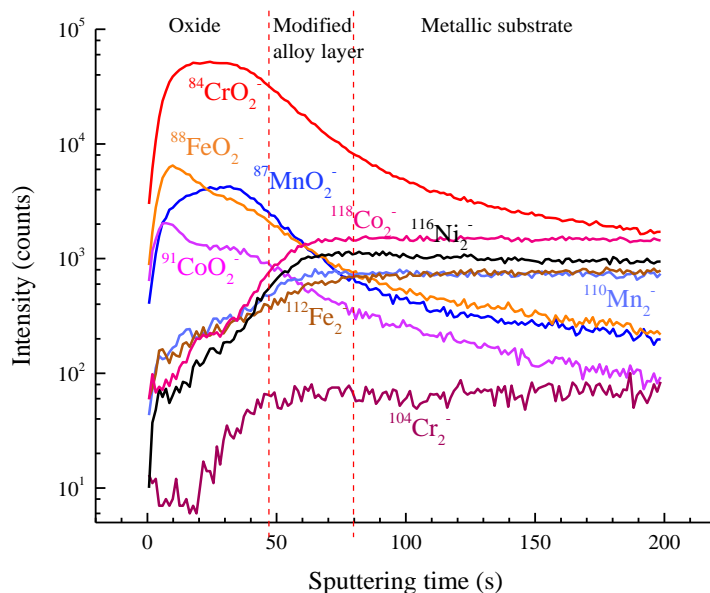


**Fig.7** ToF-SIMS depth profiles for the passive film formed on the HEA at 400 mV/SCE in 0.05M H<sub>2</sub>SO<sub>4</sub> (Passivation time:4600s; passive current:0.1μA/cm<sup>2</sup>)

Fig.7 shows the ToF-SIMS depth profile for the passive film formed on the CoCrFeMnNi HEA sample after passivation for 4600s in 0.05M H<sub>2</sub>SO<sub>4</sub>(aq) at 400 mV/SCE.

As previously, the depth profiles can be splitted into 3 regions corresponding to the passive film, the modified alloy and the metallic substrate. After passivation, the structure of the oxide film is not modified. The <sup>91</sup>CoO<sub>2</sub><sup>-</sup> and <sup>88</sup>FeO<sub>2</sub><sup>-</sup> signals in the outer oxide show a lower intensity, indicating a lower Co and Fe concentration; the oxides of the other elements remain unchanged. As for the modified alloy layer, a slight Ni enrichment is observed.

## 4. Discussion

In this work, XPS and ToF-SIMS have been used to determine the nature (chemical composition) and thickness of different oxides (native oxide, passive layers) formed on the surface of a CoCrFeMnNi HEA. The native oxide presents an enrichment of Cr<sup>3+</sup> (46.3 at %) and Fe<sup>3+</sup> (30.3 at%) while passive films comprise mainly Cr<sup>3+</sup> (>60%). In all cases, Ni oxide is not detected by XPS. The chromium enrichment in the oxide layer is in agreement with the

Gibbs standard free energy of formation ( $\Delta G_{298.15\text{K}}^\circ$ ) for  $\text{Cr}_2\text{O}_3$ , which is  $-1058.067\text{kJ/mol}$ , i.e. much more negative than for  $\text{Fe}_2\text{O}_3$  ( $-742.294\text{ kJ/mol}$ ),  $\text{MnO}_2$  ( $-465.138\text{ kJ/mol}$ ) and  $\text{CoO}$  ( $-214.198\text{ kJ/mol}$ ) [54].

A duplex layer covers the substrate. Fe and Co are located preferentially in the outer layer, Mn in the inner layer. Cr is distributed in the whole film. A modified alloy layer, enriched in Ni, is observed under the oxide film.

After exposure of the alloy covered by the native oxide to acidic aqueous solution at OCP, the CoCrFeMnNi HEA shows a marked dissolution of Fe oxide from the film, in agreement with others [57]. The amounts of Cr oxide and hydroxide in the film are increased after immersion for 60 min. This is explained by the slow dissolution rate of Cr compared to Fe oxide in the acid media [22, 38]. Despite the dissolution of species in sulfuric acid, the thickness of the film is increased after immersion. There is a balance between dissolution of the species and growth of the oxide which seems to bring a stationary thickness after ~30 min of immersion. The thickening of the oxide film is observed by both XPS and ToF-SIMS measurements.

The passivity of the HEA at different passive potentials (200mV, 400mV and 600mV) has been studied. The XPS characterization has shown that the passivation potential has a weak effect on the composition and thickness of the oxide layer and modified alloy layer. The studied passive films are found to be enriched in Cr species, particularly Cr oxide, compared to the native oxide film. The contents of Mn and Co oxides in the passive films are similar to that in the native oxide film. Much less Fe oxide is observed in the passive film after passivation, which is consistent with the high dissolution of Fe oxide in the acidic solution. The total thickness for the passive films is found to be 1.6-1.7 nm, which is of the same order of magnitude as the thickness of the passive film (1.5-2 nm) on stainless steel after passivation in sulfuric acid [22, 58]. During passivation at 400 mV in sulfuric acid, the main modification of the composition observed in the passive film is the increase of Cr oxide and decrease of Cr hydroxide. Considering that the total content of Cr species (Cr oxide and hydroxide) in the film is stationary, the passivation process is correlated to the transformation of Cr hydroxide into Cr oxide. This transformation process is also responsible for the decrease of passive current. This passivation mechanism has been already proposed by Marcus et al. [38] for the passivation of stainless steel. The thickness of the film is maintained at 1.6-1.7 nm, hence the passivation time has no significant effect on the thickness of the passive film, which has already been verified by Maurice et al. [22] for Fe-17Cr-14.5Ni-2.3Mo stainless steel.

## 5. Conclusions

XPS, ToF-SIMS and electrochemical measurements were combined in order to study the corrosion behavior of the equiatomic CoCrFeMnNi high entropy alloy, with emphasis on characterization of the native oxide and passive films. A new XPS approach based on the analysis of 3p core level spectra has been developed. The parameters for fitting the 3p core level peaks of pure metals were used as reference for fitting the XPS 3p spectra for the oxide covered high entropy alloy. The decomposition of Cr 3p core level peaks into oxide and hydroxide have been verified by fitting also the Cr 2p spectra.

For all studied oxide films (native oxide and passive films), a duplex structure is observed. Cr<sup>3+</sup> is distributed in the whole film, while Fe and Co oxides are located preferentially in the outer layer and Mn oxide in the inner layer. Ni is not observed in the oxide layer. A modified metallic layer is observed under the oxide, with a significant enrichment of nickel.

During immersion in sulfuric acid at OCP, a selective dissolution of iron oxide combined with an increase of the chromium hydroxide is clearly demonstrated. Mn and Co oxide contents and locations in the film are not significantly modified.

After passivation of the HEA, an increase of chromium content is observed in the passive film. The transformation from Cr hydroxide to Cr oxide (by dehydroxylation) is observed for increasing passivation time.

## Declaration of Competing Interest

The authors declare that they have no known competing financial interests or personal relationships that could have appeared to influence the work reported in this paper.

## Author Statement

Luntao Wang: Methodology, Investigation, Formal analysis, Writing - original draft

Dimitri Mercier: Conceptualization, Writing - review & editing, Supervision

Sandrine Zanna: Investigation, Methodology, Validation

Antoine Seyeux: Investigation, Methodology, Validation

Mathilde Laurent-Brocq: Writing - review, Investigation

Loïc Perrière: Investigation

Ivan Guillot: Investigation, Writing - review

Philippe Marcus: Conceptualization, Writing - review & editing, Supervision.

All authors contributed to the interpretation of the results and to the writing of the paper.

## Data availability statement

The datasets generated for this study are available on request to the corresponding author.

## Acknowledgements

This project has received funding from the European Research Council (ERC) under the European Union's Horizon 2020 research and innovation program (ERC Advanced grant no. 741123). Région île-de-France is acknowledged for partial funding of the ToF-SIMS equipment. China Scholarship Council (CSC) is acknowledged for the scholarship to the first author (No. 201706460018).

## References

- [1] D.B. Miracle, O.N. Senkov, A critical review of high entropy alloys and related concepts, *Acta Mater.* 122 (2017) 448-511.
- [2] Y. Zhang, T.T. Zuo, Z. Tang, M.C. Gao, K.A. Dahmen, P.K. Liaw, Z.P. Lu, Microstructures and properties of high-entropy alloys, *Prog. Mater. Sci.* 61 (2014) 1-93.
- [3] O. Senkov, J. Miller, D. Miracle, C. Woodward, Accelerated exploration of multi-principal element alloys with solid solution phases, *Nat. Commun.* 6 (2015) 6529.
- [4] Y. Zhang, *High-Entropy Materials: A Brief Introduction*, Springer 2019.
- [5] T. Nagase, P.D. Rack, J.H. Noh, T. Egami, In-situ TEM observation of structural changes in nano-crystalline CoCrCuFeNi multicomponent high-entropy alloy (HEA) under fast electron irradiation by high voltage electron microscopy (HVEM), *Intermetallics* 59 (2015) 32-42.
- [6] G. Bracq, M. Laurent-Brocq, L. Perrière, R. Pirès, J.-M. Joubert, I. Guillot, The fcc solid solution stability in the Co-Cr-Fe-Mn-Ni multi-component system, *Acta Mater.* 128 (2017) 327-336.
- [7] Z. Wu, H. Bei, F. Otto, G.M. Pharr, E.P. George, Recovery, recrystallization, grain growth and phase stability of a family of FCC-structured multi-component equiatomic solid solution alloys, *Intermetallics* 46 (2014) 131-140.
- [8] G. Bracq, M. Laurent-Brocq, C. Varvenne, L. Perrière, W. Curtin, J.-M. Joubert, I. Guillot, Combining experiments and modeling to explore the solid solution strengthening of high and medium entropy alloys, *Acta Mater.* 177 (2019) 266-279.
- [9] M. Feuerbacher, T. Lienig, C. Thomas, A single-phase bcc high-entropy alloy in the refractory Zr-Nb-Ti-V-Hf system, *Scr. Mater.* 152 (2018) 40-43.
- [10] J. Couzinié, G. Dirras, L. Perrière, T. Chauveau, E. Leroy, Y. Champion, I. Guillot, Microstructure of a near-equimolar refractory high-entropy alloy, *Mater. Lett.* 126 (2014) 285-287.
- [11] L. Liliensten, J.-P. Couzinié, L. Perrière, A. Hocini, C. Keller, G. Dirras, I. Guillot, Study of a bcc multi-principal element alloy: Tensile and simple shear properties and underlying deformation mechanisms, *Acta Mater.*

142 (2018) 131-141.

[12] O.N. Senkov, G. Wilks, J. Scott, D.B. Miracle, Mechanical properties of Nb<sub>25</sub>Mo<sub>25</sub>Ta<sub>25</sub>W<sub>25</sub> and V<sub>20</sub>Nb<sub>20</sub>Mo<sub>20</sub>Ta<sub>20</sub>W<sub>20</sub> refractory high entropy alloys, *Intermetallics* 19 (2011) 698-706.

[13] B. Cantor, I.T.H. Chang, P. Knight, A.J.B. Vincent, Microstructural development in equiatomic multicomponent alloys, *Mater. Sci. Eng.: A* 375-377 (2004) 213-218.

[14] B. Gludovatz, A. Hohenwarter, D. Catoor, E.H. Chang, E.P. George, R.O. Ritchie, A fracture-resistant high-entropy alloy for cryogenic applications, *Science* 345 (2014) 1153-1158.

[15] B. Schuh, F. Mendez-Martin, B. Völker, E.P. George, H. Clemens, R. Pippan, A. Hohenwarter, Mechanical properties, microstructure and thermal stability of a nanocrystalline CoCrFeMnNi high-entropy alloy after severe plastic deformation, *Acta Mater.* 96 (2015) 258-268.

[16] Y. Zhao, D.-H. Lee, M.-Y. Seok, J.-A. Lee, M. Phaniraj, J.-Y. Suh, H.-Y. Ha, J.-Y. Kim, U. Ramamurty, J.-i. Jang, Resistance of CoCrFeMnNi high-entropy alloy to gaseous hydrogen embrittlement, *Scr. Mater.* 135 (2017) 54-58.

[17] Y. Shi, B. Yang, P. Liaw, Corrosion-resistant high-entropy alloys: A review, *Metals* 7 (2017) 43.

[18] Y. Qiu, S. Thomas, M.A. Gibson, H.L. Fraser, N. Birbilis, Corrosion of high entropy alloys, *NPJ Mater. Degrad.* 1 (2017) 15.

[19] Z. Tang, L. Huang, W. He, P.K. Liaw, Alloying and processing effects on the aqueous corrosion behavior of high-entropy alloys, *Entropy* 16 (2014) 895-911.

[20] M.-H. Tsai, J.-W. Yeh, High-entropy alloys: a critical review, *Materials Research Letters*, 2 (2014) 107-123.

[21] E. Gardin, S. Zanna, A. Seyeux, A. Allion-Maurer, P. Marcus, Comparative study of the surface oxide films on lean duplex and corresponding single phase stainless steels by XPS and ToF-SIMS, *Corros. Sci.* 143 (2018) 403-413.

[22] V. Maurice, H. Peng, L.H. Klein, A. Seyeux, S. Zanna, P. Marcus, Effects of molybdenum on the composition and nanoscale morphology of passivated austenitic stainless steel surfaces, *Faraday Discuss.* 180 (2015) 151-170.

[23] V. Maurice, P. Marcus, Progress in corrosion science at atomic and nanometric scales, *Prog. Mater. Sci.* 95 (2018) 132-171.

[24] V. Maurice, W. Yang, P. Marcus, XPS and STM Study of Passive Films Formed on Fe- 22Cr (110) Single-Crystal Surfaces, *Journal of the Electrochemical Society*, 143 (1996) 1182-1200.

[25] Y. Dou, S. Han, L. Wang, X. Wang, Z. Cui, Characterization of the passive properties of 254SMO stainless steel in simulated desulfurized flue gas condensates by electrochemical analysis, XPS and ToF-SIMS, *Corros. Sci.* (2019) 108405.

[26] S. Fajardo, I. Llorente, J.A. Jiménez, J. Bastidas, D.M. Bastidas, Effect of Mn additions on the corrosion behaviour of TWIP Fe-Mn-Al-Si austenitic steel in chloride solution, *Corros. Sci.* 154 (2019) 246-253.

[27] S. Peissl, G. Mori, H. Leitner, R. Ebner, S. Eglsäer, Influence of chromium, molybdenum and cobalt on the corrosion behaviour of high carbon steels in dependence of heat treatment, *Mater. Corros.* 57 (2006) 759-765.

[28] C.P. Lee, C.C. Chang, Y.Y. Chen, J.W. Yeh, H.C. Shih, Effect of the aluminium content of Al<sub>x</sub>CrFe<sub>1.5</sub>MnNi<sub>0.5</sub> high-entropy alloys on the corrosion behaviour in aqueous environments, *Corros. Sci.* 50 (2008) 2053-2060.

[29] Y.-F. Kao, T.-D. Lee, S.-K. Chen, Y.-S. Chang, Electrochemical passive properties of Al<sub>x</sub>CoCrFeNi (x= 0, 0.25, 0.50, 1.00) alloys in sulfuric acids, *Corros. Sci.* 52 (2010) 1026-1034.

[30] C.-M. Lin, H.-L. Tsai, Evolution of microstructure, hardness, and corrosion properties of high-entropy Al<sub>0.5</sub>CoCrFeNi alloy, *Intermetallics* 19 (2011) 288-294.

[31] Y.-J. Hsu, W.-C. Chiang, J.-K. Wu, Corrosion behavior of FeCoNiCrCux high-entropy alloys in 3.5% sodium chloride solution, *Mater. Chem. Phys.* 92 (2005) 112-117.

- [32] X.-L. Shang, Z.-J. Wang, Q.-F. Wu, J.-C. Wang, J.-J. Li, J.-K. Yu, Effect of Mo Addition on Corrosion Behavior of High-Entropy Alloys CoCrFeNiMo<sub>x</sub> in Aqueous Environments, *Acta Metall. Sin. Engl.* 32 (2019) 41-51.
- [33] K.F. Quiambao, S.J. McDonnell, D.K. Schreiber, A.Y. Gerard, K.M. Freedy, P. Lu, J.E. Saal, G.S. Frankel, J.R. Scully, Passivation of a corrosion resistant high entropy alloy in non-oxidizing sulfate solutions, *Acta Mater.* 164 (2019) 362-376.
- [34] A. Rodriguez, J.H. Tylczak, M. Ziomek-Moroz, Corrosion Behavior of CoCrFeMnNi High-Entropy Alloys (HEAs) Under Aqueous Acidic Conditions, *ECS Trans.* 77 (2017) 741-752.
- [35] G. Laplanche, U. Volkert, G. Eggeler, E. George, Oxidation behavior of the CrMnFeCoNi high-entropy alloy, *Oxid. Met.* 85 (2016) 629-645.
- [36] M. Laurent-Brocq, A. Akhatova, L. Perrière, S. Chebini, X. Sauvage, E. Leroy, Y. Champion, Insights into the phase diagram of the CrMnFeCoNi high entropy alloy, *Acta Mater.* 88 (2015) 355-365.
- [37] F. Di Franco, A. Seyeux, S. Zanna, V. Maurice, P. Marcus, Effect of High Temperature Oxidation Process on Corrosion Resistance of Bright Annealed Ferritic Stainless Steel, *J. Electrochem. Soc.* 164 (2017) C869-C880.
- [38] V. Maurice, W. Yang, P. Marcus, X- Ray photoelectron spectroscopy and scanning tunneling microscopy study of passive films formed on (100) Fe- 18Cr- 13Ni single- crystal surfaces, *J. Electrochem. Soc.* 145 (1998) 909-920.
- [39] A. Machet, A. Galtayries, P. Marcus, P. Combrade, P. Jolivet, P. Scott, XPS study of oxides formed on nickel-base alloys in high- temperature and high- pressure water, *Surf. Interface Analysis* 34 (2002) 197-200.
- [40] P. Marcus, M.E. Bussell, XPS study of the passive films formed on nitrogen-implanted austenitic stainless steels, *Appl. Surf. Sci.* 59 (1992) 7-21.
- [41] M.C. Biesinger, B.P. Payne, A.P. Grosvenor, L.W.M. Lau, A.R. Gerson, R.S.C. Smart, Resolving surface chemical states in XPS analysis of first row transition metals, oxides and hydroxides: Cr, Mn, Fe, Co and Ni, *Appl. Surf. Sci.* 257 (2011) 2717-2730.
- [42] M. Aronniemi, J. Sainio, J. Lahtinen, Chemical state quantification of iron and chromium oxides using XPS: the effect of the background subtraction method, *Surf. Sci.* 578 (2005) 108-123.
- [43] T. Yamashita, P. Hayes, Analysis of XPS spectra of Fe<sup>2+</sup> and Fe<sup>3+</sup> ions in oxide materials, *Appl. Surf. Sci.* 254 (2008) 2441-2449.
- [44] B. Payne, M. Biesinger, N. McIntyre, X-ray photoelectron spectroscopy studies of reactions on chromium metal and chromium oxide surfaces, *J. Electron Spectrosc. Relat. Phenom.* 184 (2011) 29-37.
- [45] A.M. Salvi, J.E. Castle, J.F. Watts, E. Desimoni, Peak fitting of the chromium 2p XPS spectrum, *Appl. Surf. Sci.* 90 (1995) 333-341.
- [46] E. Ünveren, E. Kemnitz, S. Hutton, A. Lippitz, W. Unger, Analysis of highly resolved x- ray photoelectron Cr 2p spectra obtained with a Cr<sub>2</sub>O<sub>3</sub> powder sample prepared with adhesive tape, *Surf. Interface Analysis* 36 (2004) 92-95.
- [47] S. Doniach, M. Sunjic, Many-electron singularity in X-ray photoemission and X-ray line spectra from metals, *J. Phys. C: Solid State Phys.* 3 (1970) 285.
- [48] J.W. Gadzuk, M. Šunjić, Excitation energy dependence of core-level x-ray-photoemission-spectra line shapes in metals, *Phys. Rev. B* 12 (1975) 524.
- [49] N.D. Stepanov, D.G. Shaysultanov, G.A. Salishchev, M.A. Tikhonovsky, E.E. Oleynik, A.S. Tortika, O.N. Senkov, Effect of V content on microstructure and mechanical properties of the CoCrFeMnNiV<sub>x</sub> high entropy alloys, *J. Alloys Compd.* 628 (2015) 170-185.
- [50] J. He, W. Liu, H. Wang, Y. Wu, X. Liu, T. Nieh, Z. Lu, Effects of Al addition on structural evolution and tensile properties of the FeCoNiCrMn high-entropy alloy system, *Acta Mater.* 62 (2014) 105-113.



- [51] J.H. Scofield, Hartree-Slater subshell photoionization cross-sections at 1254 and 1487 eV, *J. Electron Spectrosc. Relat. Phenom.* 8 (1976) 129-137.
- [52] S. Tanuma, C.J. Powell, D.R. Penn, Calculations of electron inelastic mean free paths. II. Data for 27 elements over the 50–2000 eV range, *Surf. Interface Analysis* 17 (1991) 911-926.
- [53] L. Wang, A. Seyeux, P. Marcus, Thermal stability of the passive film formed on 316L stainless steel surface studied by ToF-SIMS, *Corros. Sci.* (2019) 108395.
- [54] I. Barin, *Thermochemical data of pure substances*, VCH, (1989).
- [55] H.E. Evans, D.A. Hilton, R.A. Holm, Chromium-depleted zones and the oxidation process in stainless steels, *Oxid. Met.* 10 (1976) 149-161.
- [56] C. Leygraf, G. Hultquist, Initial oxidation stages on Fe-Cr(100) and Fe-Cr(110) surfaces, *Surf. Sci.* 61 (1976) 69-84.
- [57] H. Luo, Z. Li, A.M. Mingers, D. Raabe, Corrosion behavior of an equiatomic CoCrFeMnNi high-entropy alloy compared with 304 stainless steel in sulfuric acid solution, *Corros. Sci.* 134 (2018) 131-139.
- [58] Z. Wang, F. Di-Franco, A. Seyeux, S. Zanna, V. Maurice, P. Marcus, Passivation-induced physicochemical alterations of the native surface oxide film on 316L austenitic stainless steel, *J. Electrochem. Soc.* 166 (2019) C3376-C3388.